CHALMERS

Direct Current Leakage in CNF-MIM Capacitors with High-k Dielectric and TiN Electrode

Degree Project in Electrical Engineering

Hanna Bergman

DEPARTMENT OF SPACE, EARTH AND ENVIRONMENT
CHALMERS UNIVERSITY OF TECHNOLOGY
Gothenburg, Sweden 2025
www.chalmers.se

DEGREE PROJECT 2025

Direct Current Leakage in CNF-MIM Capacitors with High-k Dielectric and TiN Electrode

HANNA BERGMAN

CHALMERS

Department of Space, Earth and Environment
CHALMERS UNIVERSITY OF TECHNOLOGY
Gothenburg, Sweden 2025

Direct Current Leakage in CNF-MIM Capacitors with High-k Dielectric and TiN Electrode
HANNA BERGMAN

© Hanna Bergman, 2025

Supervisor: Farzan Ghavanini, Smoltek
Examiner: Arto Heikkilä, Chalmers University of Technology

Degree project 2025
Department of Space, Earth and Environment
Chalmers University of Technology
SE-412 96 Gothenburg
Sweden
Telephone +46 31 772 1000

Typeset in LaTeX
Gothenburg, Sweden 2025

Direct Current Leakage in CNF-MIM Capacitors with High-k Dielectric and TiN Electrode
HANNA BERGMAN
Department of Space, Earth and Environment
Chalmers University of Technology

Abstract

This study examines leakage currents in metal-insulator-metal (MIM) capacitors with TiN / $ZrO_2/Al_2O_3/ZrO_2$ / TiN stacks. Seven samples were analyzed with oxide thicknesses of 11 nm, 15 nm, and 20 nm. The samples either lacked annealing or were annealed at 400 °C, 500 °C, or 600 °C. Current density was plotted as a function of electic field in room temperature. The data was then re-plotted in linear Poole-Frenkel (PF) and Fowler-Nordheim (FN) form to identify the dominant leakage cause. Additionally, elevated temperature measurements were conducted in order to determine the temperature dependence of the leakage current.

For the 20 nm films, a 400 °C anneal produced PF-type leakage at low and medium electric field strength that later changed to trap-assisted tunneling (TAT) at higher bias. Raising the anneal to 500 °C and 600 °C reduced the PF dominance, resulting in TAT alone explained the leakage. However, annealing at 600 °C showed a slight increase in leakage, indicating an that higher anneal induces more defects. No evidence of FN tunneling was found, consistent with the relatively thick dielectric. In the thinner 11–15 nm devices all three samples showed strong temperature dependence and optical dielectric constants that matched PF theory, indicating that PF emission is the main leakage cause. The 15 nm capacitor annealed at 500 °C showed low leakage up to 300 MV/m, outperforming the 11 nm stacks.

The results show that leakage can be reduced by combining a moderate oxide thickness (≥15 nm) with a 500 °C post-deposition anneal. The work also outlines a practical method of voltage and temperature sweeps, that is useful for diagnosing leakage mechanisms in MIM capacitors.

Keywords: MIM capacitor, Leakage, Poole-Frenkel, Fowler-Nordheim, Tunneling, CNF.

Direct Current Leakage in CNF-MIM Capacitors with High-k Dielectric and TiN Electrode
HANNA BERGMAN
Department of Space, Earth and Environment
Chalmers University of Technology

Sammanfattning

Denna studie undersöker läckströmmar i metal-insulator-metal (MIM) kondensatorer med TiN / $ZrO_2/Al_2O_3/ZrO_2$ / TiN lager. Sju olika kondensatorer valdes ut, med oxidetjocklekar 11 nm, 15 nm och 20 nm. Proverna genomgick antingen ingen glödgning alls eller glödgades vid 400 °C, 500 °C eller 600 °C. Strömtätheten plottades som funktion av elektrisk fältstyrka vid rumstemperatur, därefter ritades samma data om i linjär Poole-Frenkel (PF) och Fowler-Nordheim (FN) form för att identifiera den dominerande läckmekanismen. Mätningar vid förhöjd temperatur genomfördes också för att fastställa läckströmmens temperaturberoende.

För 20 nm proverna gav en glödgning på 400 °C en PF typisk läckning vid låga och medelhöga fältstyrkor, som övergick till trap-assisted tunnling (TAT) vid högre bias. När glödgningen ökades till 500 °C och 600 °C så minskade PF dominansen, så att läckningen förklaras av TAT. Glödgning på 600 °C gav dock en liten ökning av läckströmmen, vilket indikerar att högre glödgning kan introducera fler defekter. FN tunnling kunde inte påvisas i något prov, vilket är förenligt med det relativt tjocka dielektrumet. I de tunnare 11-15 nm proverna så visade alla ett starkt temperaturberoende och optiska dielektriska konstanter som stämmer överens med PF teori, vilket tyder på att PF emission är huvudorsaken till läckaget.

Resultatet visar att läckström kan minskas genom att kombinera en måttlig oxidtjocklek ($\geq$15 nm) med en glödgning av 500 °C. Arbetet beskriver dessutom en praktisk metod med spänning- och temperatursvep som är användbar för att diagnosera läckmekanismer i MIM-kondensatorer. Rapporten är skriven på engelska.

Nyckelord: MIM kondensator, läckström, Poole-Frenkel, Fowler-Nordheim, Tunnling, CNF.

Acknowledgements

I would like to thank Farzan Ghavanini at Smoltek for giving me the opportunity to work on this project and for his guidance throughout. I am also grateful to Vir Manh, Qi Li, Andreas Westlund and Arto Heikkilä for their support and helpful advice.

Hanna Bergman, Gothenburg, June 2025

List of Acronyms

Below is the list of acronyms that have been used throughout this thesis:

BDV	Breakdown Voltage
CNF-MIM	Carbon nanofiber metal insulator metal
DC	Direct current
DRAM	Dynamic Random Access memory
FN	Fowler-Nordheim
MIM	Metal insulator Metal
PF	Poole-Frenkel
RF	Radio Frequency
TAT	Trap-Assisted tunneling

Nomenclature

Below is the nomenclature of variables that have been used throughout this thesis.

Variables

ϕ_B	Schottky Barrier
ϵ_r	Optic dielectric constant
ϵ_0	Dielectric constant in vacuum (permittivity in vacuum)
h	Planck's constant
$\hbar$	Reduced Planck's constant
m^*	Electron's effective mass
q	Elementary charge
E	Electric field
A^*	Effective Richardson constant
k_B	Boltzmann's constant
A	Area
V	Voltage
ϕ_T	Trap level depth
N_c	Effective density of states in conduction band
μ	Carrier mobility

Contents

List of Acronyms **viii**

Nomenclature **ix**

List of Figures **xiii**

List of Tables **xv**

1 Introduction **1**
- 1.1 Background . . . 1
- 1.2 Aims and Goals . . . 1
- 1.3 Limitations . . . 1
- 1.4 Environmental and ethical aspects . . . 2

2 Theory **3**
- 2.1 Metal-Insulator-Metal Capacitor . . . 3
- 2.2 Important Characteristics of a Capacitor . . . 3
  - 2.2.1 Dielectric Constant . . . 4
  - 2.2.2 Annealing . . . 5
  - 2.2.3 ZAZ structure . . . 5
- 2.3 Leakage Current . . . 5
  - 2.3.1 Schottky Emission . . . 6
  - 2.3.2 Poole-Frenkel Emission . . . 7
  - 2.3.3 Fowler-Nordheim Tunneling . . . 7
  - 2.3.4 Trap-Assisted Tunneling . . . 8

3 Methods **9**
- 3.1 Samples . . . 9
- 3.2 Measurement Approach . . . 9
  - 3.2.1 Voltage Sweep . . . 10
  - 3.2.2 Current measurements at different temperatures . . . 10
    - 3.2.2.1 What is an Arrhenius plot? . . . 10
- 3.3 General Considerations for Leakage Current . . . 11
- 3.4 Linearizing the Expressions . . . 11
  - 3.4.1 Linear Poole-Frenkel model . . . 11
  - 3.4.2 Linear FN Tunneling . . . 12
- 3.5 Data Analysis . . . 12

4 Results **13**
4.1 Voltage sweeps . . . 13
4.2 Poole-Frenkel Plots . . . 16
4.3 Fowler-Nordheim Plots . . . 20
4.4 Arrhenius plots . . . 24

5 Conclusion **27**
5.1 Guidelines for Analysing Leakage in MIM Capacitors . . . 28
5.2 Reflection . . . 28

List of Figures

2.1 Band diagram Schottky Emission 6
2.2 Band diagram Poole-Frenkel Emission 7
2.3 Band diagram FN tunneling 8

4.1 Current density, 20 nm, as-deposited to 600 °C anneal. 14
4.2 Current density, closer view of sample 2 and 3 14
4.3 Current density, 11 nm, 400 °C vs. 500 °C. 15
4.4 Current density, 15 nm, 500 °C. 15
4.5 PF, 20 nm, 400 °C 16
4.6 PF, 20 nm, 500 °C 17
4.7 PF, 20 nm, 600 °C 17
4.8 PF, 20 nm, as-deposited 18
4.9 PF, 11 nm, 400 °C 18
4.10 PF, 11 nm, 500 °C 19
4.11 PF, 15 nm, 500 °C 19
4.12 FN, 20 nm, 400 °C 20
4.13 FN, 20 nm, 500 °C 21
4.14 FN, 20 nm, 600 °C 21
4.15 FN, 20 nm, as-deposited 22
4.16 FN, 11 nm, 400 °C 22
4.17 FN, 11 nm, 500 °C 23
4.18 FN, 15 nm, 500 °C 23
4.19 Arrhenius, 20 nm samples 24
4.20 Arrhenius, 11 nm samples 25
4.21 Arrhenius, 15 nm sample 25

List of Tables

3.1 Samples characteristics 9
5.1 Summary of Derived Parameters and Characteristics 27

1
Introduction

1.1 Background

Smoltek is a company focused on developing process technology within semiconductor and hydrogen industries, with a focus on carbon nanofibers [1].

Carbon nanofiber metal–insulator-metal (CNF-MIM) capacitors from Smoltek have a large capacitance while maintaining a small area, making them attractive for DRAM cells, RF circuits, and power-management chips [1]. The high-k dielectric (high relative permittivity) helps to achieve a high capacitance density, but it can also cause direct current (DC) leakage that wastes power and shortens device life.

This project focuses on investigating the mechanisms and factors that contribute to DC leakage in CNF-MIM capacitors with high-k dielectrics. Through a combination of an in-depth literature review and experimental studies, the research aims to enhance understanding of leakage behavior in CNF-MIM capacitors and develop strategies to mitigate it.

1.2 Aims and Goals

The project aims to investigate DC leakage mechanisms in CNF-MIM capacitors with high-k dielectrics and Titanium Nitride (TiN) electrodes. The results will include:

1. A detailed understanding of DC leakage mechanisms.
2. Experimental data linking leakage currents to fabrication parameters.
3. Recommendations for minimizing leakage in CNF-MIM capacitors.

1.3 Limitations

While this thesis aims to provide valuable insights into DC leakage mechanisms in CNF-MIM capacitors, the following limitations should be considered:

- The fabrication of the CNF-MIM capacitors is conducted exclusively by the Smoltek staff. This limits control over fabrication variables.
- Theoretical models will be used for data fitting; these models may not capture all complexities of real-world conduction mechanisms due to simplifications or assumptions.
- The analysis is limited to the tools and equipment available at Smoltek.

1.4 Environmental and ethical aspects

Leakage current in capacitors lets charge slowly escape through the dielectric, the supply must then continuously replace this lost charge which raises the standby power consumption. Part of the wasted energy will be converted into heat inside the device, which can cause damage to other components. Studying leakage currents in capacitors is useful in order to create more energy efficient and sustainable electronic devices in the future.

The material for high-k oxides is often extracted through mining in various regions, in order for an ethical manufacturing process the labour conditions in these mines should be considered. It is also important to consider possible negative environmental impacts that come with mining.

2

Theory

This chapter provides a description of theoretical elements relevant for this thesis.

2.1 Metal-Insulator-Metal Capacitor

Metal insulator metal (MIM) capacitors are constructed by sandwiching a very thin dielectric layer between two conductive (metal) layers. This dielectric layer is typically on the order of 10 nm thick, which allow for a high capacitance density in a small area [2].

2.2 Important Characteristics of a Capacitor

A capacitor is an electrical component consisting of two conducting plates separated by an insulating layer called the dielectric. Capacitors store energy in an electric field. The characteristics of the capacitor are partly determined by the permittivity (dielectric constant) of the dielectric layer. The permittivity can be expressed as:

$$\epsilon = \epsilon_r \epsilon_0 \tag{2.1}$$

where ϵ_r is the material's relative permittivity and ϵ_0 ($8.85418 \cdot 10^{-12}$ F/m) the permittivity for vacuum [3],[4]. When a capacitor is connected to a DC voltage source, the conducting plates will store the charge $\pm q$. The charge is proportional to the voltage and the area in the following expression:

$$q = \epsilon \frac{A}{d} V \tag{2.2}$$

where q is the charge, V is the voltage, A is the area and d is the distance between plates. When a voltage is applied over a parallel plate capacitor the resulting electric field has the following expression:

$$E = \frac{\mathrm{V}}{d} \tag{2.3}$$

if the electric field varies in time, displacement current results [4]:

$$i_d = \frac{d(\epsilon \phi_E)}{dt} = \frac{dq}{dt} \tag{2.4}$$

where ϕ_E is the electric flux

$$\Phi_E = \oint_S \vec{E} \cdot d\vec{A} \tag{2.5}$$

The displacement current is the current that is typically used in circuit theory when discussing currents through a capacitor ($i(t) = C\frac{d(v(t))}{dt}$). In an ideal case this would be the only current, however, due to non ideal properties real world capacitor also have additional leakage current due to a non zero conductivity of the dielectric.

Current is often given as current density, which describes how much electric current flows through an area in each point in space and has the following formulation [4]:

$$J = \frac{I}{A} \tag{2.6}$$

For the leakage current $J = \sigma E$. Here σ is the conductivity of the material, leakage in a capacitor means that $\sigma \neq 0$, this lead to ohmic losses. The leakage turns the stored energy into thermal energy at the power level per m^3:

$$\sigma E^2 \tag{2.7}$$

The ability of a capacitor to store charge is described by its capacitance and can be written as [4]:

$$C = \frac{q}{\Delta \mathrm{V}} \tag{2.8}$$

For parallel plate capacitors, the area and dielectric thickness can be used to expand on this formulation, resulting in [3],[4]:

$$C = \frac{\epsilon_r \epsilon_0 A}{d} \tag{2.9}$$

Capacitance can be transformed into capacitance density in a similar manner:

$$\frac{C}{A} = \frac{\epsilon_r \epsilon_0}{d} \tag{2.10}$$

Higher capacitance means a capacitor is able to let through higher i_d [4].

The stored energy in a capacitors is [4]:

$$\frac{1}{2}CV^2 \tag{2.11}$$

2.2.1 Dielectric Constant

When an electric field is applied across a metal, the electrons are able to move freely which quickly works to cancel out the internal electric field. Dielectric materials, however, do not have free charges that can move throughout the material. Instead, the electrons are tightly bound to their respective atoms or molecules. When an external field is applied these bound charges shift slightly, resulting in electronic polarization. This displacement forms electric dipoles throughout the material. The effect of these dipoles is a partial cancellation of the applied electric field, and a materials dielectric constant is a variable that describes how well that material reduces the electric field. A high-k dielectric constant means the material creates stronger dipoles, leading to a higher ϵ_r and gives more reduction of the electric field which also enables a capacitor to store more energy [5].

2.2.2 Annealing

Annealing is a thermal treatment which can improve the quality of the dielectric and interface layers of a capacitor. During deposition and processing, the dielectric layer can develop defects such as oxygen vacancies, dangling bonds, and other structural irregularities [2]. These defects can act as charge traps or unwanted conduction paths, which contribute to increased leakage current and degraded electrical performance. The annealing process provides thermal energy that allows atoms in the material to move and reorganize into a more stable and ordered structure. This helps to reduce the number of defects and creates a more uniform dielectric structure. However, too much heat may have the opposite effect, causing degradation of the metal electrodes and underlying substrate [2].

2.2.3 ZAZ structure

This study will focus on capacitors with a dielectric stack made of two different materials, zirconium dioxide (ZrO_2) and aluminum oxide (Al_2O_3). The structure is arranged so that ZrO_2 is placed next to the both the top and bottom titanium nitride (TiN) electrodes, while Al_2O_3 is placed between the two ZrO_2 layers, hence the term "ZAZ".

ZrO_2 has a high dielectric constant, which helps increase capacitance density. However, it has a smaller bandgap than Al_2O_3, which makes it more prone to leakage currents. By combining these materials in a layered structure it is possible to utilize the high dielectric constant of ZrO_2 as well as the large bandgap of Al_2O_3 in order to achieve a capacitor with a large capacitance density and low leakage current.

2.3 Leakage Current

Leakage current is one of the main challenges when designing MIM capacitors and the choice of dielectric material can have a significant impact on leakage current. For many years, silicon dioxide (SiO_2) was a widely used dielectric material due to its good insulating properties. However, SiO_2 has a relatively low dielectric constant of 3.9 [6] which limits capacitance density.

As electronic devices become smaller, there has been an increasing need for smaller capacitors. One way to keep the capacitance high while maintaining a small area is to make the dielectric layer thinner. However, making the insulating layer thinner will increase the probability that charge carriers are able to pass through. This creates a trade-off between storing more charge and preventing leakage [6].

To solve this problem, researches have turned to high-k dielectric materials, which have a higher dielectric constant than SiO_2. These materials are able to store a higher charge, even with a thicker dielectric layer. Unlike SiO_2, which is mostly made of covalent bonds, many high-k materials have ionic or mixed bonding, where atoms are surrounded by more oxygen atoms. This is advantageous since it makes the material more polar, however, this bonding structure can also make the materiel more prone to defects [6].

At absolute zero, an ideal dielectric has all of its electrons in the valence band with

no electrons in the conduction band [6]. At any temperature above this, however, there is a chance that some charge carriers gain enough energy and are able to jump into the conduction band, causing leakage. Leakage mechanisms in dielectrics can be grouped into two main types:

1. Injection-limited conduction mechanisms
2. Bulk-limited conduction mechanisms

Injection-limited conduction depend on the contact between electrode and dielectric [6], and include Schottky emission, Fowler-Nordheim tunneling and direct tunneling. Bulk-limited conduction depends only on the properties of the dielectric and include Poole-Frenkel emission and trap-assisted tunneling.

2.3.1 Schottky Emission

Schottky emission, sometimes referred to as thermionic emission, happens when electrons gain enough thermal energy so that they can overcome the potential energy barrier at the interface of metal and dielectric. This barrier can be further lowered by something called the Schottky effect [6]. Schottky emission typically becomes more prominent at high temperatures [6]. The expression for the current density due to Schottky emission is as follows [6]:

$$J_{Schottky} = A^{*}T^{2}\exp[\frac{-q(\phi_B - \sqrt{\frac{qE}{4\pi\epsilon_r\epsilon_0}})}{k_B T}] \tag{2.12}$$

where

$$A^{*} = \frac{4\pi q k_B^2 m^{*}}{h^3} \tag{2.13}$$

Here A^{*} is the effective Richardson constant, m^{*} is the effective electron mass in the dielectric, T is the absolute temperature, q is the electronic charge, ϕ_B is the Schottky barrier height, E is the electric field across the dielectric, k_B is the Boltzmann's constant, h is the Planck's constant, ϵ_0 is the permittivity in vacuum and ϵ_r is the optical dielectric constant [6].

Figure 2.1 show a simplified band diagram of Schottky emission, with energy in y-direction.

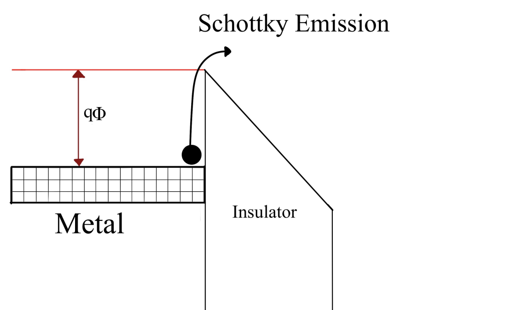

Figure 2.1: Band diagram Schottky Emission

2.3.2 Poole-Frenkel Emission

Poole-Frenkel (PF) emission is similar to Schottky emission, however, in PF emission, electrons are thermally excited from trap states within the insulating oxide, whereas in Schottky emission, electrons acquire thermal energy to overcome the potential barrier at the electrode-insulator interface [6]. In PF emission, the electrons do not have enough energy to overcome the whole potential barrier, however, they are able to overcome the potential barrier associated with the trap and can then "hop" between trap sites and thus transition into the conduction band [6].

When an electric field is applied, it lowers the energy required for an electron to escape from the trap by reducing the height of the potential barrier [6]. As a result, electrons need less thermal energy to be excited into the conduction band, which increases the emission rate. The current density in PF emission follows an exponential dependence on the square root of the electric field, which helps distinguish it experimentally from other conduction mechanisms. However, it can still be challenging to distinguish this emission mechanism from Schottky emission, as both processes often occur simultaneously under similar conditions.

The expression for PF emission is as follows [6]

$$J_{PF} = q\mu N_c E \exp[-\frac{q(\phi_T - \sqrt{\frac{qE}{\pi\epsilon_r\epsilon_0}})}{k_B T}] \tag{2.14}$$

Where μ is the carrier mobility, N_c the effective density of states in conduction band and ϕ_T the trap depth. Figure 2.2 show a simplified band diagram of Poole-Frenkel emission, with energy in y-direction.

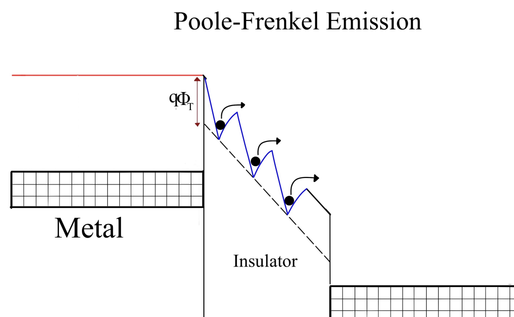

Figure 2.2: Band diagram Poole-Frenkel Emission

2.3.3 Fowler-Nordheim Tunneling

In quantum mechanics, particles have a wave-like behavior that allows them to pass through barriers even when their they do not have enough energy to overcome the barrier height. This phenomenon is known as tunneling, and it is the basis for Fowler-Nordheim (FN) tunneling [7]. At high electric fields, the energy barrier becomes thinner an more triangular in shape, which increases the probability that electrons can tunnel through it. This leads to an increase in leakage current, especially in thinner dielectrics. FN tunneling is more likely to occur when the dielectric layer is very thin and the applied voltage is high enough that energy bands bend

and form a triangular potential barrier. The current density in FN tunneling can be written as:

$$J_{FN} = \alpha_{FN} \frac{E^2}{\phi_B} exp\left(-\frac{b_{FN}\phi_B^{3/2}}{E}\right) \tag{2.15}$$

where

$$\alpha_{FN} = \frac{q^3}{16\pi^2\hbar} \tag{2.16}$$

$$b_{FN} = \frac{4}{3}\frac{(2m^*)^{1/2}}{q\hbar} \tag{2.17}$$

In equation 2.15 ϕ_B is the energy of the barrier, not the potential. Figure 2.3 show a simplified band diagram of Fowler-Nordheim tunneling, with energy in y-direction.

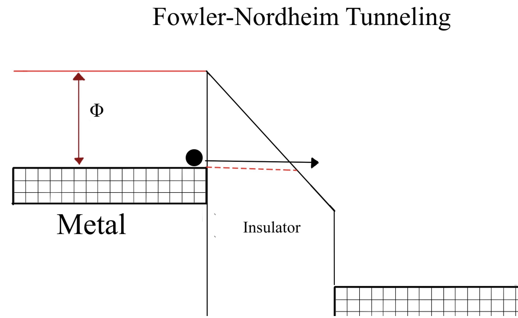

Figure 2.3: Band diagram FN tunneling

2.3.4 Trap-Assisted Tunneling

Trap-assisted tunneling (TAT) is a leakage current model that is typically used when PF emission, FN tunneling or Schottky emission are unable to explain the leakage behavior. TAT occurs when electrons tunnel through the dielectric by stepping between traps or defect states within the dielectric [8].

3

Methods

The measurements for this study were done with the following equipment:

- Keysight B2961b, a low-noise power supply.
- Keithley 6430, a Sub-Femtoamp Remote Source Meter.
- Thermal chuck and probe station.

3.1 Samples

The following samples are analyzed in this study has area $A = 4.1 \cdot 10^{-8}$ m^2, with additional characteristics listed in table 3.1:

Table 3.1: Samples characteristics

Sample	Thickness	$ZrO_2/Al_2O_3/ZrO_2$ (nm)	Annealing	Max voltage
1	20 nm	5/10/5	400 °C	10 V
2	20 nm	5/10/5	500 °C	10 V
3	20 nm	5/10/5	600 °C	10 V
4	20 nm	5/10/5	none	10 V
5	11 nm	5/1/5	400 °C	3 V
6	11 nm	5/1/5	500 °C	3 V
7	15 nm	5/5/5	500 °C	6 V

In order to isolate the behavior of the dielectric stack, this study has set aside the CNF treated samples and worked with "bare" MIM capacitors that share the same bottom electrode, oxide chemistry, thickness and top electrode as the CNF ones. This was done because possible chemical interaction between the CNF and high-k film during anneal can further complicate the leakage structure.

3.2 Measurement Approach

Two types of measurements were performed:

1. Voltage sweep at room temperature.
2. Fixed voltage current measurements across varying temperatures.

3.2.1 Voltage Sweep

The voltage sweep was used to evaluate how leakage current evolves with increasing electric field. Since mechanisms like FN tunneling and TAT are heavily field driven, observing the leakage behavior below breakdown provides insight into which mechanism is dominant.

The maximum voltage sweep for each sample was set based on its previously measured BDV to avoid dielectric breakdown. Since the samples have different thickness and structure the BDV is not the same for all samples. All sweeps used:

1. Step size: 0.1 V
2. Settling time per step: 30 seconds

3.2.2 Current measurements at different temperatures

To distinguish between field-dependent and thermally activated leakage mechanisms, current was also measured at a fixed voltage across multiple temperatures. Samples 1-4 were mounted on a shared wafer using thermal tape and measured at the same time. This was due to time constraints and a desire for the measuring conditions to be as equal as possible for comparison. Samples 5-7 were measured two at a time and were not placed on a wafer.

Measuring conditions were:

1. Temperatures: 23 °C, 40 °C, 70 °C, 100 °C.
2. Voltage:
   - Samples 1–4: 8 V.
   - Samples 5–6: 3 V.
   - Sample 7: 6 V & 5 V.
3. Settling time: 120 s, longer due to thermal stabilization needs.

Unlike the voltage sweep measurements, this setup required elevated temperatures which was achieved using a thermal chuck supported by an air compressor. However, activating the air compressor introduced electrical interference. Each time it engaged, it provided the capacitor with a small charge, resulting in an artificial increase in measured leakage current.

To mitigate this issue, a different measurement setup was used. The Keithley source meter was configured to both apply the voltage and measure the resulting current, and the Keysight power supply used in previous measurement was removed. Additionally, a 1 MΩ series resistor was added to suppress noise. While this setup helped reduce interference, it introduced a known limitation, the measurement system itself contributed a small leakage current. As a result, these temperature-dependent measurement are slightly less accurate than the voltage sweep data. However, the setup remains effective for evaluating trends in leakage in relation to temperature, which is useful for identifying dominant conduction mechanisms.

3.2.2.1 What is an Arrhenius plot?

An Arrhenius plot is useful model for visualizing how a thermally activated process depends on temperature. It plots the natural logarithm as function of the reaction rate, against the inverse of the absolute temperature. The model can be expressed

as follows:

$$\text{Reaction rate} = \text{Constant} \cdot \exp(\frac{\text{-Activation energy}}{k_b T}) \tag{3.1}$$

In this study the quantity $\frac{J}{E}$ takes the role of the reaction rate. This model is useful in determining if PF or Schottky emission is a leading leakage mechanism, both these theories have an exponential dependence on temperature that can be expressed as an Arrhenius plot.

3.3 General Considerations for Leakage Current

Measuring leakage current in capacitors requires consideration of several factors in order to ensure the accuracy and reliability of the results. As soon as a voltage is applied, the capacitor draws a large current to charge up [9]. This initial current is much higher than the actual leakage current and does not reflect the steady-state behavior of the device.

After the capacitor has charged, a smaller current known as dielectric absorption can still be observed [9]. This happens because the molecules in the dielectric layer continue to slowly adjust and redistribute trapped charges, causing a gradual current flow even after the initial charging is complete [9].

3.4 Linearizing the Expressions

In order to identify the contributing leakage mechanism, the corresponding theoretical equations are first expressed in a linearized form. The experimentally measured data are then plotted against these linearized expressions, and deviations from linearity suggest another dominating mechanism is responsible.

3.4.1 Linear Poole-Frenkel model

In order to evaluate if the leakage current is dominated by PF emission, the expression for PF emission must first be linearized. First we set $q\mu N_c = J_0$ and rewrite the expression as follows

$$\ln \frac{J}{E} = \ln J_0 - \frac{q\phi_T}{k_B T} + \frac{q\sqrt{\frac{qE}{\pi\epsilon_r\epsilon_0}}}{k_B T} \tag{3.2}$$

If PF emission is the dominating leakage mechanism then the measured data of $\ln \frac{J}{E}$ over $\sqrt{E}$ should be linear.

$$y = \ln\left(\frac{J}{E}\right) \quad \text{and} \quad x = \sqrt{E}.$$

$\frac{J}{E}$ describes σ, therefore this plot shows the natural logarithm of the materials conductivity over $\sqrt{E}$.

The slope of this expression is given by:

$$Slope_{\mathrm{PF}} = \frac{q\sqrt{\dfrac{q}{\pi\,\epsilon_r\,\epsilon_0}}}{k_B\,T} \tag{3.3}$$

The intercept is:

$$\ln J_0 - \frac{q\phi_T}{k_B T} \tag{3.4}$$

3.4.2 Linear FN Tunneling

The FN emission current density formula can be linearized in order to examine experimental data [7]. In order to find the FN plot, the FN current density equation can be rewritten as:

$$\ln\left(\frac{J_{FN}}{E^2}\right) = \ln\frac{\alpha_{FN}}{\phi} - \frac{b_{FN}\phi^{3/2}}{E} \tag{3.5}$$

The linear transformation is:

$$y = \ln\left(\frac{J}{E^2}\right) \quad \text{and} \quad x = \frac{1}{E}.$$

The slope of the FN plot is given by:

$$slope_{FN} = -b_{FN}\phi^{3/2} \tag{3.6}$$

and the intercept is:

$$\ln\frac{\alpha_{FN}}{\phi}. \tag{3.7}$$

The FN plot is used to analyze the leakage behavior as a function of electric field [7]. A linear fit of the experimental data indicates that the leakage is caused by FN tunneling [7]. Deviations from the linearity plot may indicate other mechanisms such as trap-assisted tunneling or non-ideal field enhancement effects.

3.5 Data Analysis

All data was analyzed using Python, a script was created that could read and plot the resulting Excel file from the measurements. This was then plotted in J as function of E, linear PF, linear FN and Arrhenius plots.

The slopes obtained from the linear PF and FN plots are used to determine ϵ_r and ϕ_B. For a dielectric consisting of only one material, ϵ_r is often approximated by n^2, where n is the refractive index [6]. However, since the capacitors in this study consist of a ZrO_2/ Al_2O_3 stack the reasonable range for ϵ_r has to be adjusted. Earlier work on similar high-k stacks report ϵ_r values ranging from 2.0 to 5.6 [8], this interval is therefore adapted in this study. The theoretical potential barrier is estimated to be $\phi_B \approx 2.2$ eV [8].

4

Results

The following chapter will present the results from the measurements. First the current density as a function of electric field characteristics are examined, which provide a direct overview of how the leakage current depends on electric field. After this, the two linear representations of FN and PF are presented and the underlying leakage mechanism is identified. Note that the color of the plots are not consistent throughout all figures, the plotted sample is labeled in each figure.

4.1 Voltage sweeps

Figure 4.1 compares the leakage current density J against electric field E for the four 20 nm dielectric stacks (samples 1-4). Annealing at 500 °C and 600 °C suppresses the room-temperature leakage noticably compared to both the as-deposited film and 400 °C treatment. Figure 4.2 provides a closer view of the devices with the lowest leakage, and shows that going from 500 °C to 600 °C offers no further improvement. In fact, the 600 °C sample develops a slightly higher leakage at high field, suggesting the presence of traps or defects.

The thinner 11 nm devices (samples 5-6, fig 4.3) show a field-induced leakage rise that is significantly higher than that of the 20 nm set. It is also visible that the higher temperature anneal of 500 °C provide a lower leakage than that treated at 400 °C. Sample 7 in figure 4.4 (15 nm, 500 °C) sits between the two thickness groups, it is able to withstand a higher electric field than samples 5-6, and show a slower rise in leakage current.

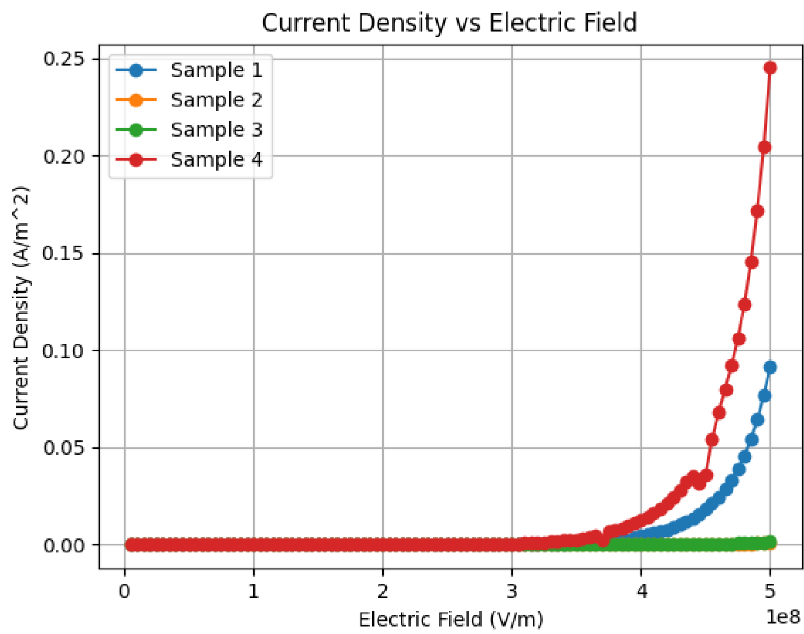

Figure 4.1: Current density, 20 nm, as-deposited to 600 °C anneal.

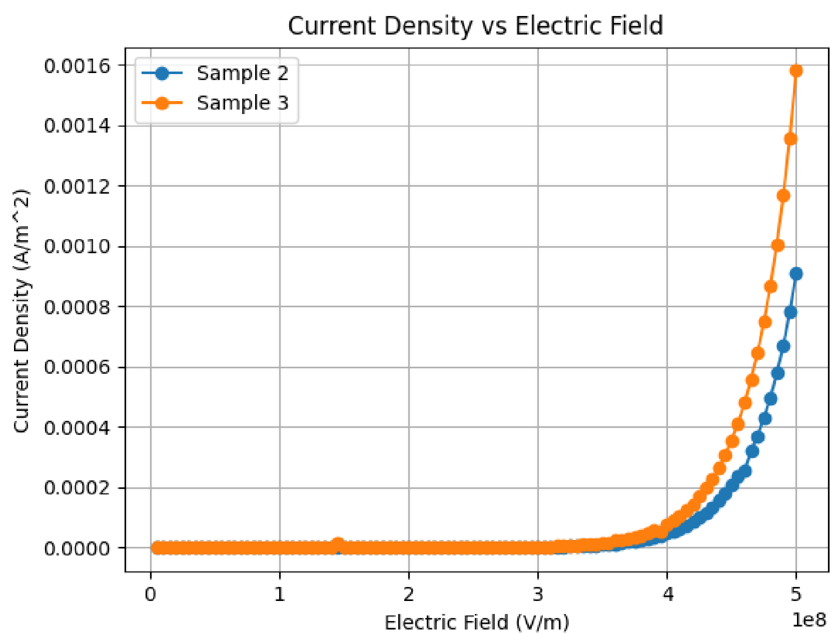

Figure 4.2: Current density, closer view of sample 2 and 3

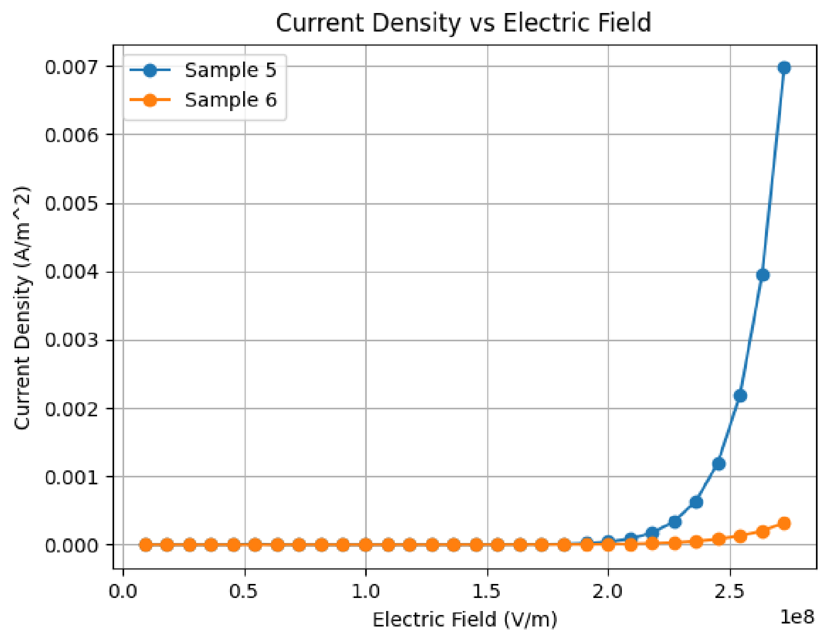

Figure 4.3: Current density, 11 nm, 400 °C vs. 500 °C.

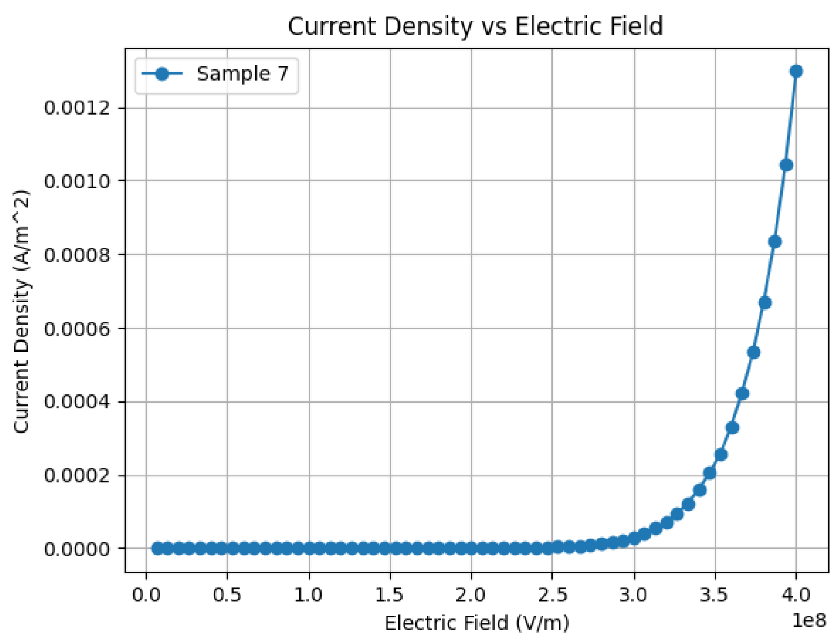

Figure 4.4: Current density, 15 nm, 500 °C.

4.2 Poole-Frenkel Plots

Figure 4.5 displays the linear Poole-Frenkel plot of sample 1, a linear fit is found in the middle E field range and gives a slope of 0.0014. The fit is the orange line, while the measured data is blue. The fit is found at the higher voltage range, since the lower bias provides too low leakage for accurate measurements. After this there is a shift in the slope, indicating a move towards another leakage transport mechanism. Equation 3.3 can be reformatted to extract the optic dielectric constant.

$$\epsilon_r = \frac{q}{\pi\epsilon_0}(\frac{q}{\text{slope}_{PF}k_B T})^2$$

For sample 1, $\epsilon_{r_1} = 4.5$, which fits well with theoretical data; indicating that PF emission could be a leading leakage mechanism. Later the leakage starts showing a higher ϵ_r, indicating a shift from PF to a tunnel mechanism. Figure 4.6 show the linear PF plot for sample 2, although, the linear PF fit is good, the extracted $\epsilon_{r_2} = 7.3$ is too high to prove PF emission. Figure 4.7 show a similar behavior as sample 2, with an equally high ϵ_r the extracted values for all samples are summarized in table 5.1.

Figure 4.9 display the linear PF plot for sample 5, and gives $\epsilon_{r_5} = 2.2$. This is lower than any previous sample, but still falls within the parameters for PF emission. From figure 4.10 the optic dielectric constant for sample 6 equals $\epsilon_{r_6} = 4.5$, which also indicates PF emission. Figure 4.11 shows the linear PF plot for sample 7, and gives $\epsilon_{r_7} = 5.2$. This is in the upper interval, however, still within PF emission range.

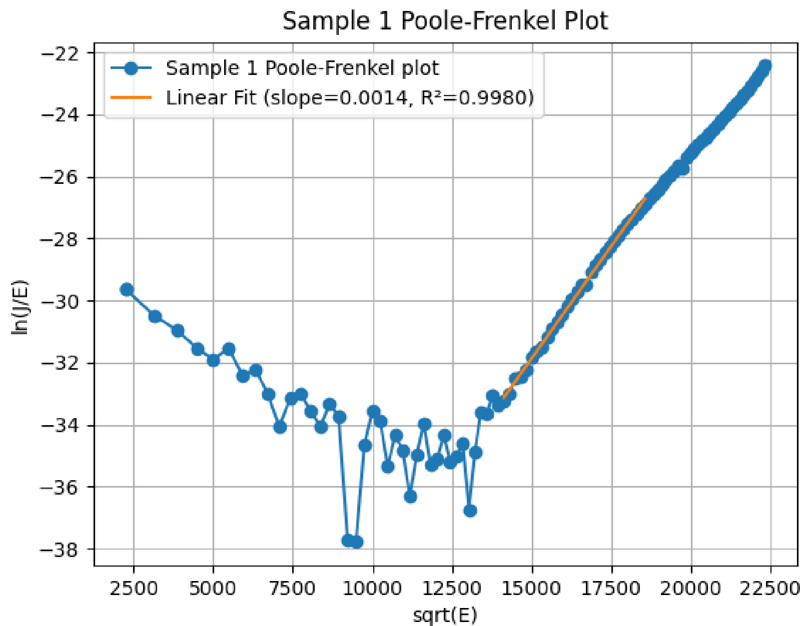

Figure 4.5: PF, 20 nm, 400 °C

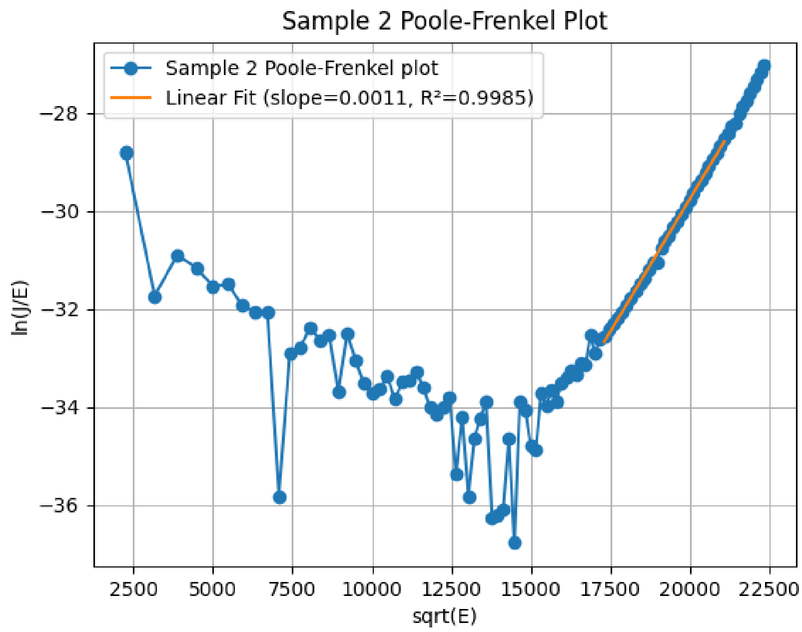

Figure 4.6: PF, 20 nm, 500 °C

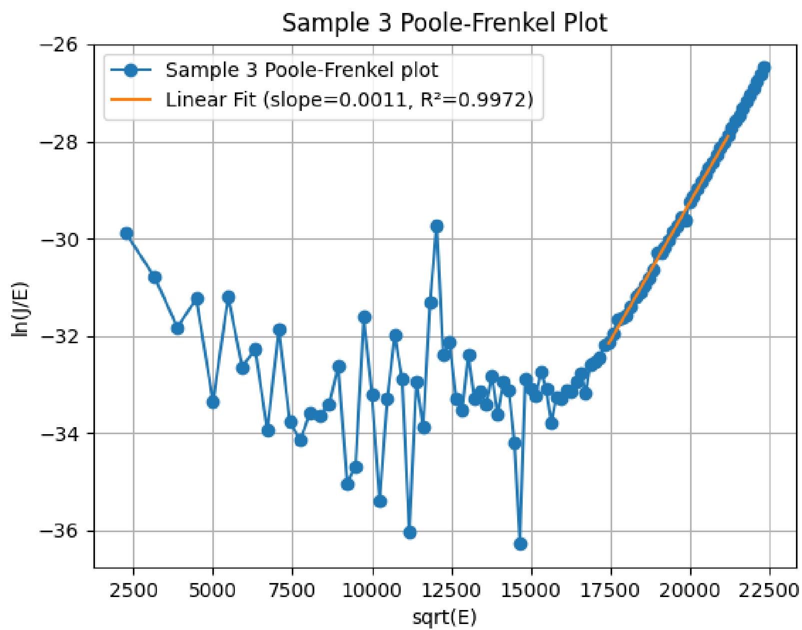

Figure 4.7: PF, 20 nm, 600 °C

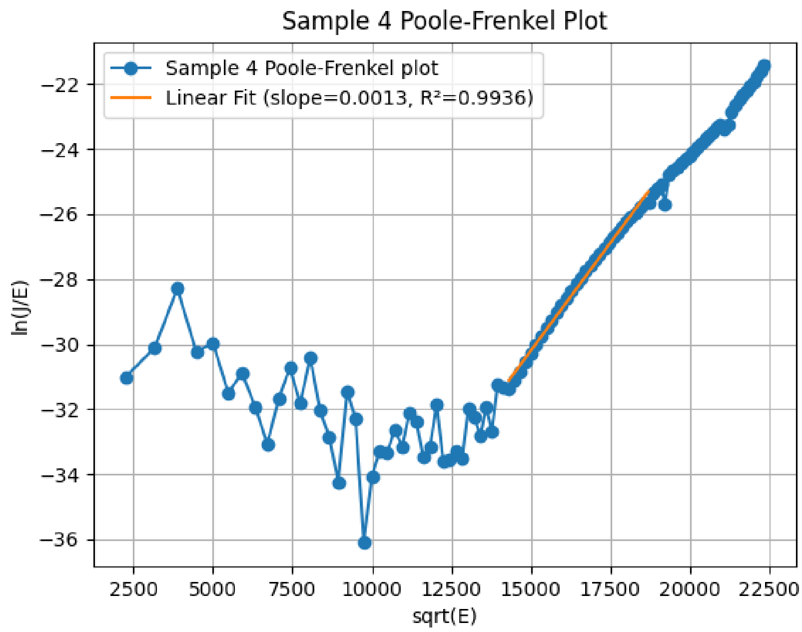

Figure 4.8: PF, 20 nm, as-deposited

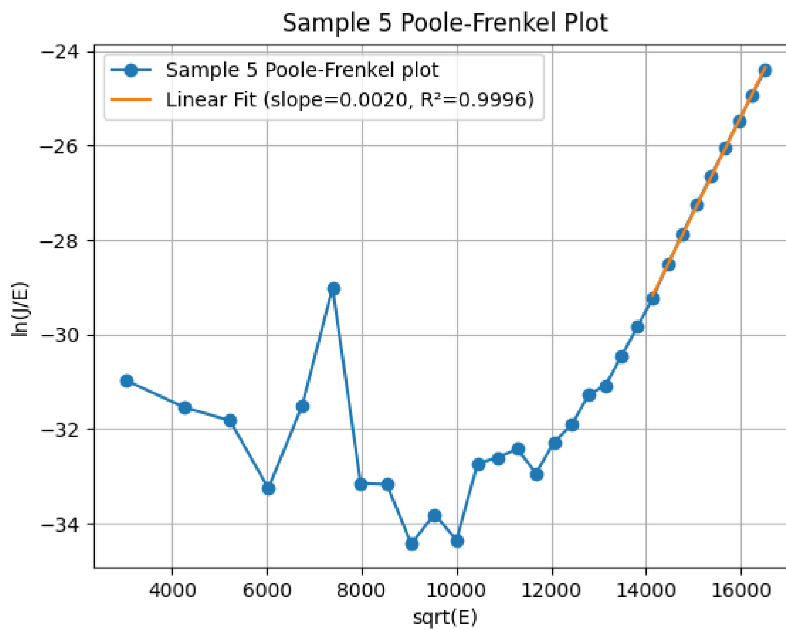

Figure 4.9: PF, 11 nm, 400 °C

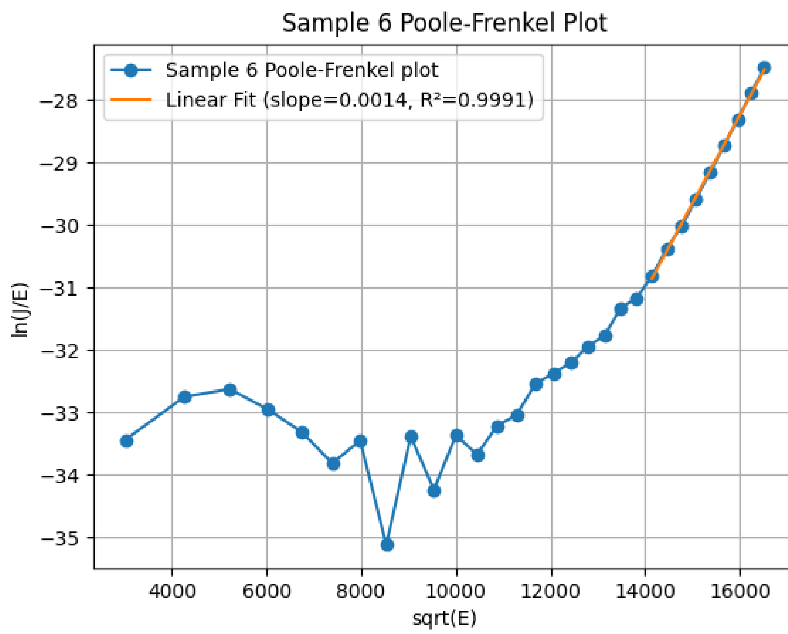

Figure 4.10: PF, 11 nm, 500 °C

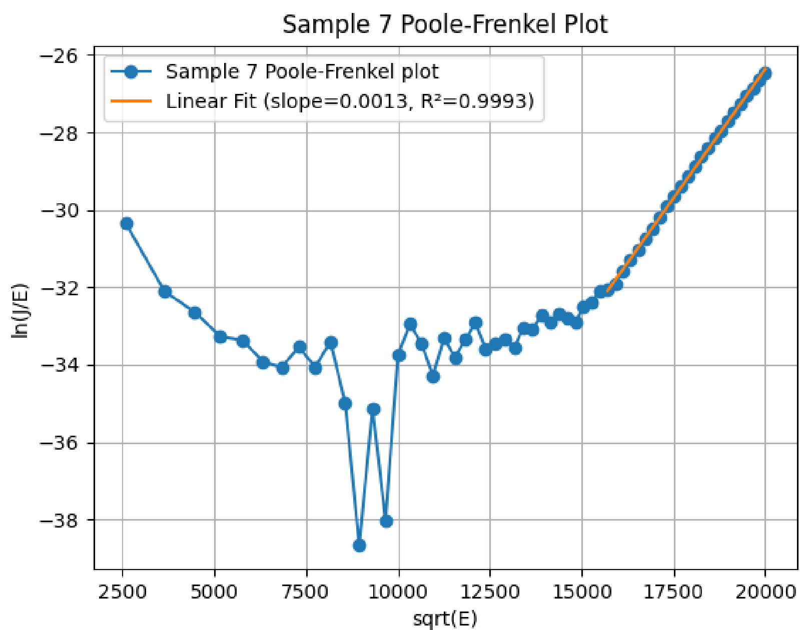

Figure 4.11: PF, 15 nm, 500 °C

4.3 Fowler-Nordheim Plots

From equation 3.6,

$$\text{slope}_{\text{FN}} = -b_{\text{FN}}\,\phi^{3/2} \quad \implies \quad \phi_B = \left(-\frac{\text{slope}_{\text{FN}}}{b_{\text{FN}}}\right)^{2/3}$$

Substituting $b_{\text{FN}} = \frac{4}{3}\frac{\sqrt{2m^*}}{q\hbar}$ gives

$$\phi_B = \left(-\frac{3q\hbar}{4\sqrt{2m^*}}\,\text{slope}_{\text{FN}}\right)^{2/3}$$

Figure 4.12 shows the linear FN plot for sample 1, using the above equation and an electron effective mass $m* = 0.4$ [10] the potential barrier for sample 1 $\phi_1 = 1.02$ eV. This is lower than the expected value of 2.2 eV, which means FN tunneling is an unlikely leakage cause for this sample. Note that the x-axis is the inverse electric field, therefore the line fit is done for data at high E, low values for $1/E$. For sample 2 and 3, the slope from figure 4.13 and 4.14 gives $\phi_2 = 1.01$ eV and $\phi_3 = 1.04$ eV. This is also too low for FN tunneling, this combined with the high ϵ_r indicates the dominance of another tunnel process, like TAT. The slope from 4.15 gives the potential barrier $\phi_4 = 1.00$ eV, which also is outside the theoretical values.

Figures 4.16, 4.17 and 4.18 show the linear FN plots for samples 5-7, all of these samples show a $\phi < 1$ eV, which makes FN tunneling an unlikely leakage transport mechanism.

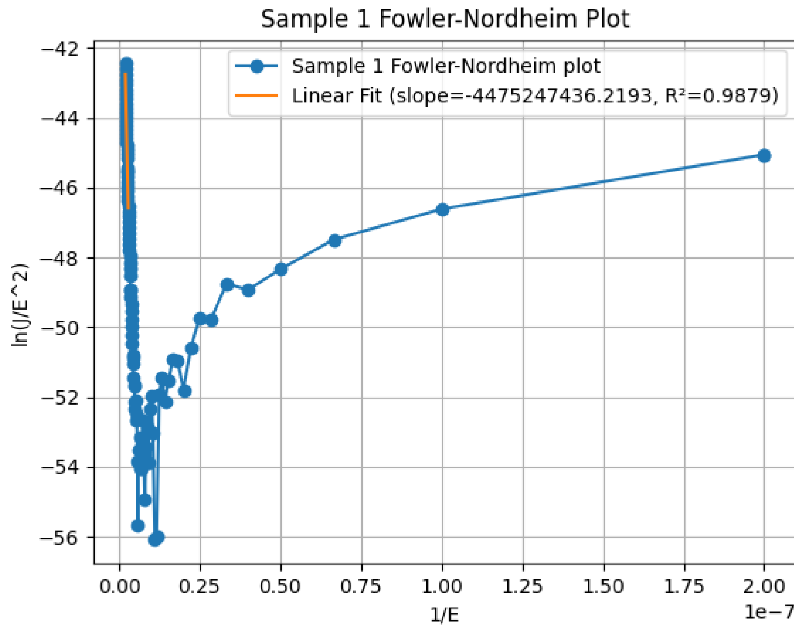

Figure 4.12: FN, 20 nm, 400 °C

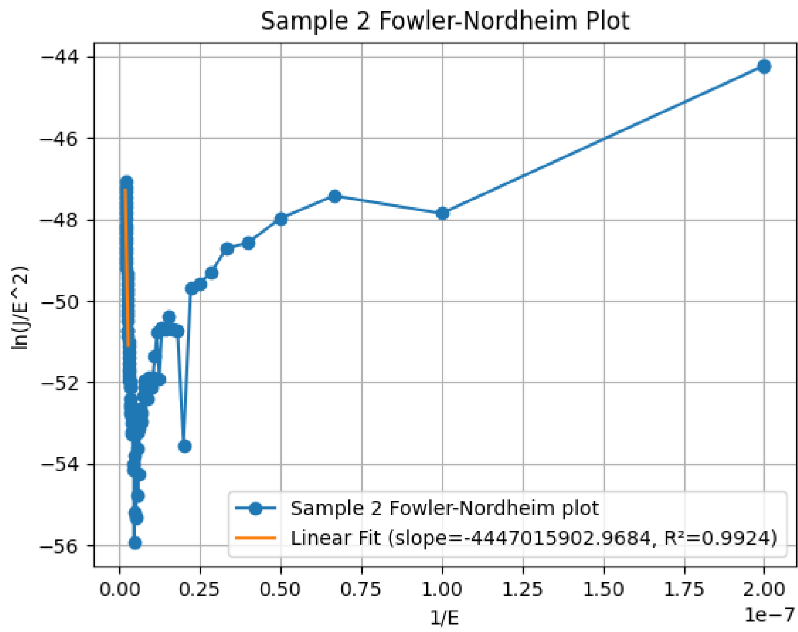

Figure 4.13: FN, 20 nm, 500 °C

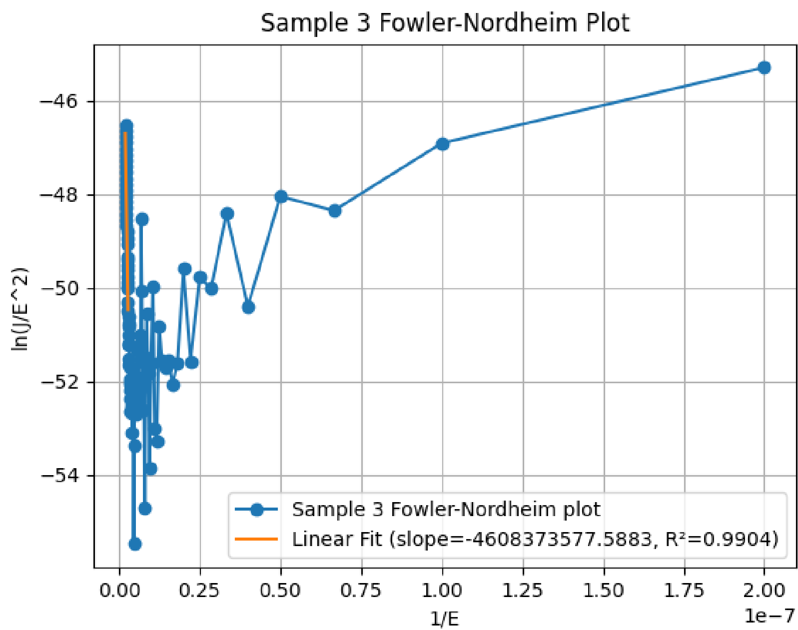

Figure 4.14: FN, 20 nm, 600 °C

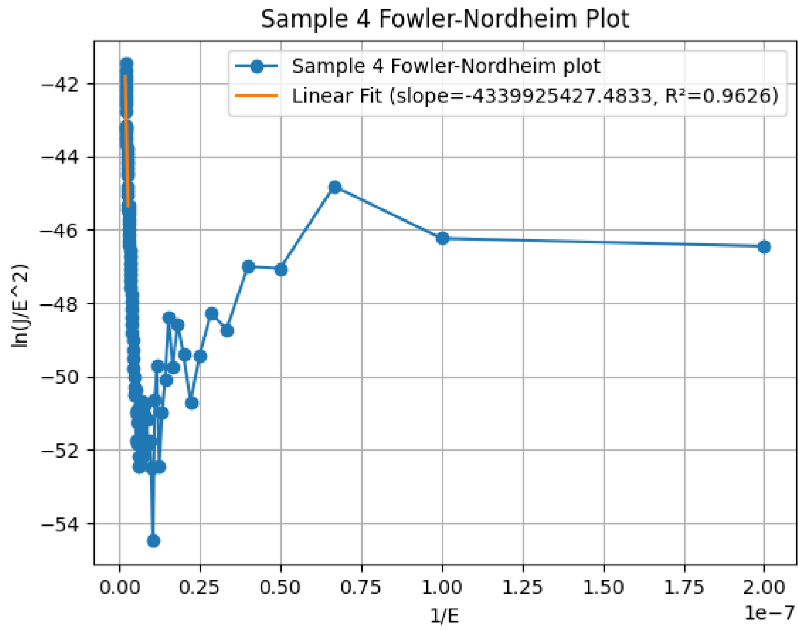

Figure 4.15: FN, 20 nm, as-deposited

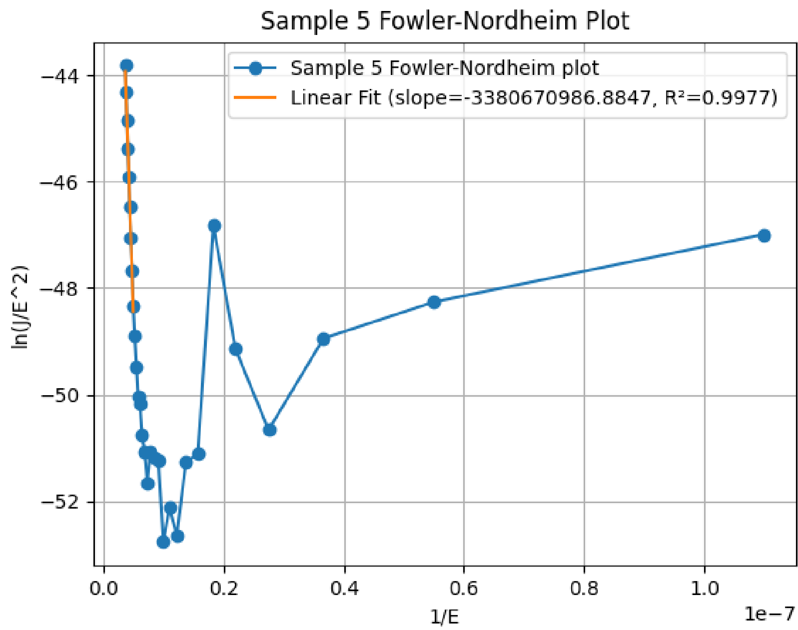

Figure 4.16: FN, 11 nm, 400 °C

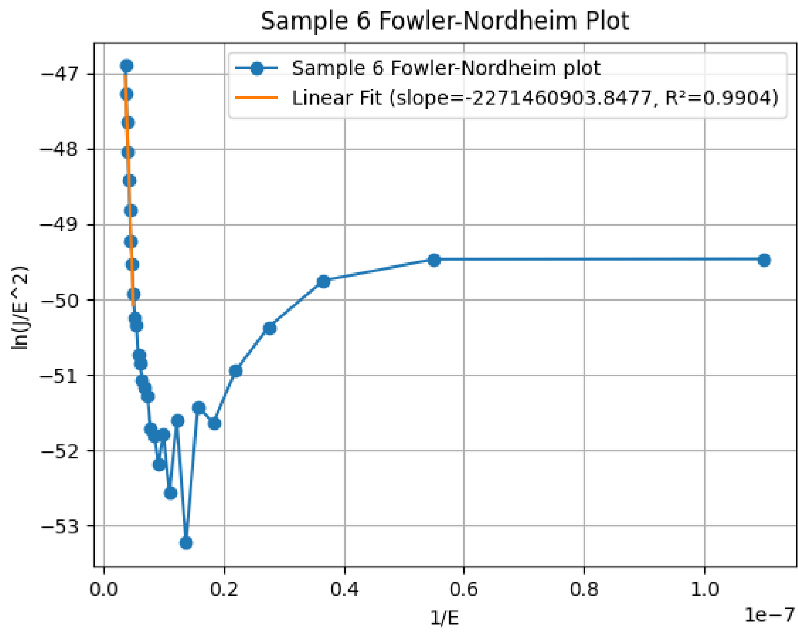

Figure 4.17: FN, 11 nm, 500 °C

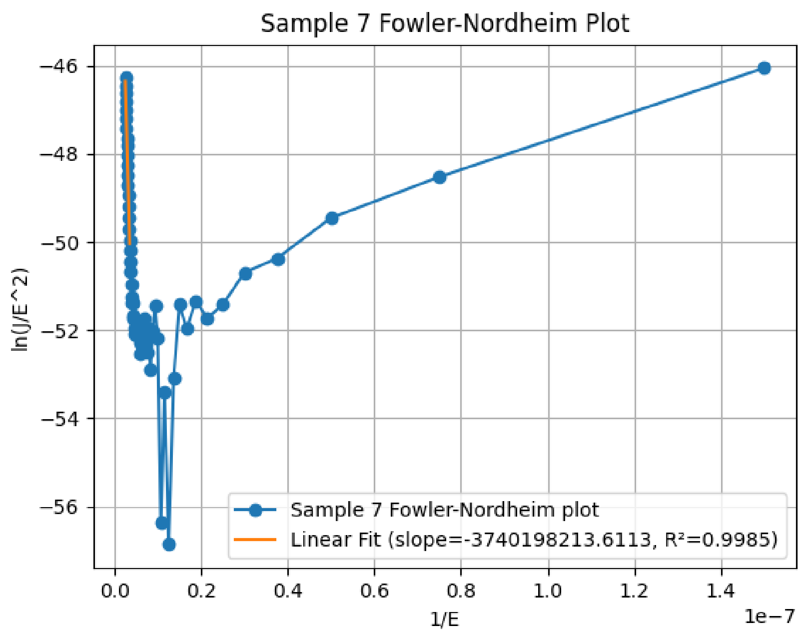

Figure 4.18: FN, 15 nm, 500 °C

4.4 Arrhenius plots

Figures 4.19, 4.20 and 4.21 display the Arrhenius plots for samples 1-3 and 5-7. For each sample there was two measurements taken, therefore there are two plots for each sample. However, in some cases to the measurements were very similar and the plots lie on top of each other. There was no valid temperature data collected from sample 4. Figure 4.19 tracks $\ln(J/E)$ versus 1000/T for three of the 20 nm samples (1-3). Sample 1 exhibits the expected temperature dependence whereas samples 2 and 3 remain relatively flat. The high temperature dependence for sample 1 fits well with PF emission, and the low dependence of samples 2-3 align with what is expected for a tunnel dominated process.

The 11 nm pair in figure 4.20 also behave in a way that is consistent with PF. For the film annealed at 500 °C (sample 6) the leakage current remains relatively flat up to 70 °C, after which it begins to climb. The film annealed at 400 °C (sample 5) is noticably more temperature sensitive, the current starts to rise steeply already at 40 °C and the device degrades at 70 °C.

For the 15 nm sample in figure 4.21 a relatively clean Arrhenius plot is obtained at 5 V. The bias had to be lowered from 6 V since the higher bias caused the device to reach breakdown at 100 °C. Sample 7 show a clear temperature dependent leakage current, indicating PF as leading mechanism. Since FN tunneling is not temperature dependent, it can be ruled out as a dominating factor for samples 1, 5, 6 and 7.

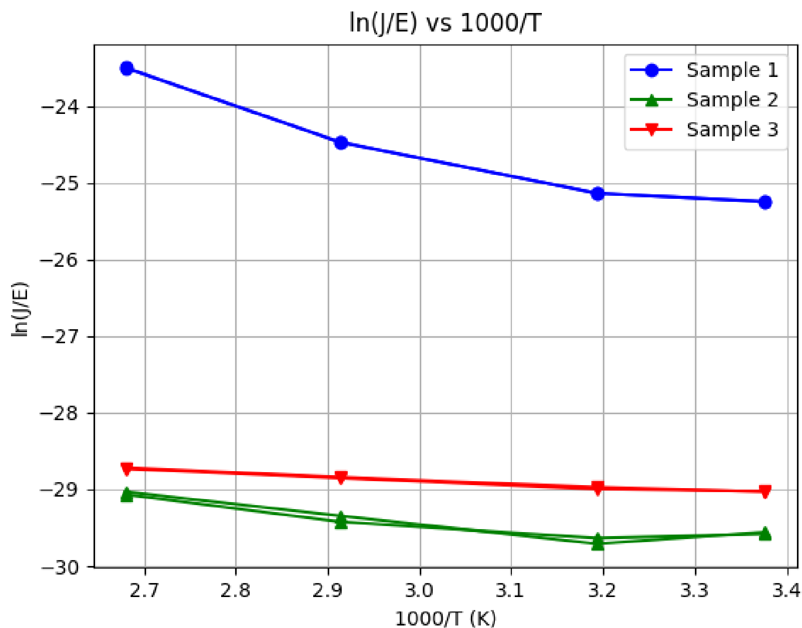

Figure 4.19: Arrhenius, 20 nm samples

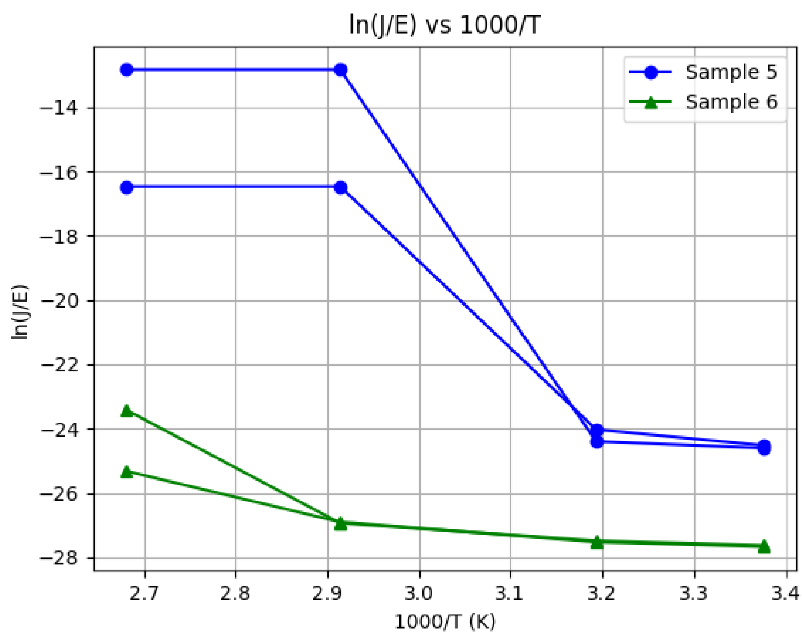

Figure 4.20: Arrhenius, 11 nm samples

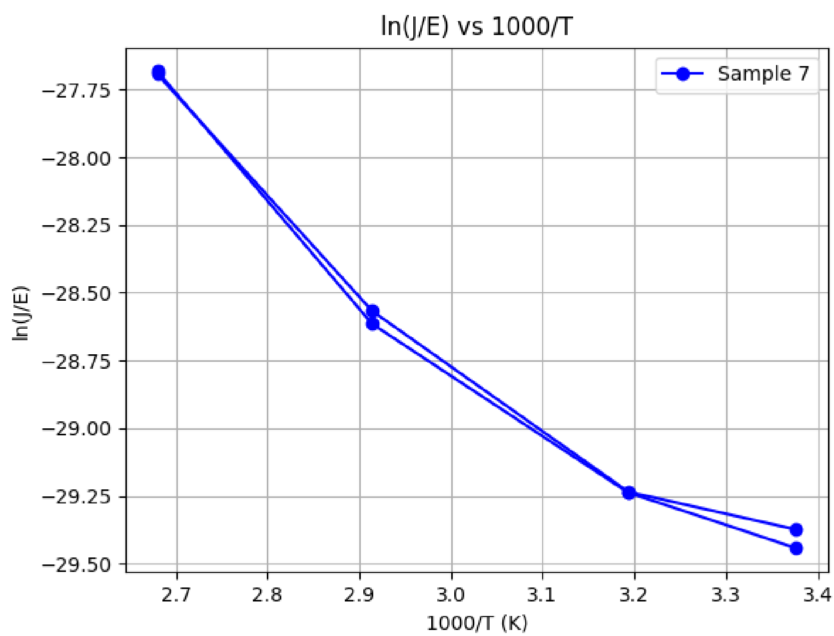

Figure 4.21: Arrhenius, 15 nm sample

5
Conclusion

The measurements show that leakage current in TiN/ZAZ/TiN MIM capacitors is strongly influenced by both the oxide thickness and the temperature of the post-deposition anneal.

For the 20 nm dielectric stack, a 400 °C anneal produces PF type conduction at low-to-moderate electric fields. As the field increases, the current gradually changes to TAT. When the same stack is annealed at 500 °C or 600 °C, the PF component is almost completely removed and the leakage is governed by TAT across the entire field range. FN tunneling is not observed in any sample. This is expected for the thicker 20 nm films because FN injection normally appears only in much thinner oxides.

For the thinner devices (samples 5-7) PF emission is the most likely leakage path, these samples show a strong temperature dependence and yield ϵ_r that agree with PF theory. Thickness therefore plays a clear role in leakage behavior, but this work cannot state with certainty whether the better performance of the thicker films is due to the added physical thickness alone or to the larger share of the Al_2O_3 layer, most likely both contribute.

Because PF emission is linked to defects that trap charge carriers, reducing those traps is important. Annealing at 500 °C greatly lowers the PF current in the 20 nm films, yet some traps remain in the thinner stacks. Even so, sample 7 performs quite well. Its leakage stays low until the electric field reaches about 300 MV/m, which is a clear improvement over samples 5 and 6.

Table 5.1: Summary of Derived Parameters and Characteristics

Sample	d (nm)	ϵ_r	ϕ_B	Mechanism
1	20	4.5	1.02	PF
2	20	7.3	1.01	TAT
3	20	7.3	1.04	TAT
4	20	5.2	1.00	PF
5	11	2.2	0.85	PF
6	11	4.5	0.65	PF
7	15	5.2	0.91	PF

5.1 Guidelines for Analysing Leakage in MIM Capacitors

Although this work focuses on a specific set of TiN/ZAZ/TiN samples, the approach it uses can serve as a practical guide for evaluating leakage in other MIM capacitors. First, leakage should be measured over a range of applied voltages, not only at a single bias point. Because each transport mechanism responds differently to the electric field, a one-point measurement does not show the leakage behavior.

Second, it is useful to measure the leakage at several different temperatures. A rise in current with temperature signals thermally activated processes such as PF or Schottky emission, whereas tunneling based mechanisms are far less temperature sensitive. By combining this data it is easier to determine the leakage mechanism for a given MIM stack.

5.2 Reflection

During the course of this study, several experimental limitations were identified. Notably, placing samples 1-4 together on the wafer led to uneven thermal contact with the chuck, meaning they were not exposed to identical temperatures during heating. While this could have been a significant issue, it has limited impact here, as the temperature measurement were not used to extract any variable data, but merely to determine whether the leakage was temperature sensitive.

Furthermore, elevated temperature measurements were attempted on sample 4, but these produced noisy plots, most likely due to poor probing contact. Unfortunately, due to time constraints, it was not possible to repeat these measurements, leaving sample 4 without an Arrhenius plot. Although this is not ideal, it is reasonable to assume that the leakage mechanism in sample 4 aligns with the observations made for sample 1, where PF emission was determined. Given that sample 4 exhibits the highest leakage current in the 20 nm batch, FN tunneling offers no explanation for the improved leakage at different anneal temperatures. This, combined with the extracted optic dielectric constant, indicates PF emission in sample 4.

Bibliography

[1] Smoltek, "Smoltek – pioneering carbon nanotechnology," 2021, [Online]. Available: https://www.smoltek.com, Accessed: Feb. 09, 2025.

[2] Saraju P. Mohanty and A. Srivastava, *Nano-CMOS and Post-CMOS Electronics: Devices and Modelling.* London, United Kingdom: The Institution of Engineering and Technology, 2016.

[3] B. Karlström, *Kretsanalys*, 2nd ed. Studentlitteratur, 2021.

[4] Hafez A. Radi and John O. Rasmussen, *Principles of Physics*, 2nd ed. Springer, 2024.

[5] Richard P. Feynman, Robert B. Leighton, and M. Sands, "The Feynman Lectures on Physics, Vol. II, Chapter 10: Dielectrics," 2013, https://www.feynmanlectures.caltech.edu/II_10.html.

[6] G. He and Z. Sun, *High-k Gate Dielectrics for CMOS Technology.* John Wiley & Sons, Inc., 2012.

[7] S.-D. Liang, *Quantum Tunneling and Field Electron Emission Theories.* New Jersey, USA: World Scientific Publishing Co., 2014.

[8] W. Weinreich, A. Shariq, K. Seidel, J. Sundqvist, A. Paskaleva, M. Lemberger, and Anton J. Bauer, "Detailed leakage current analysis of metal–insulator–metal capacitors with ZrO2, ZrO2/SiO2/ZrO2, and ZrO2/Al2O3/ZrO2."

[9] K. Technologies, "Fundamentals of leakage current measurements," Keysight Technologies, Tech. Rep. 5992-1307EN, 2015, Application Note. [Online]. Available: https://www.keysight.com/us/en/assets/7018-05086/application-notes/5992-1307.pdf.

[10] Cory K. Perkins, Melanie A. Jenkins, T.-H. Chiang, Ryan H. Mansergh, V. Gouliouk, N. Kenane, John F. Wager, John F. Conley Jr., and Douglas A. Keszler, "Demonstration of Fowler - Nordheim Tunneling in Simple Solution-Processed Thin Films," *ACS Applied Materials Interfaces*, 2018.

DEPARTMENT OF SPACE, EARTH AND ENVIRONMENT
CHALMERS UNIVERSITY OF TECHNOLOGY
Gothenburg, Sweden
www.chalmers.se